

Evaluation of tsunami wave energy generated by earthquakes in the Makran subduction zone

Amin RASHIDI^{1*}, Zaher Hossein SHOMALI^{1,2}, Denys DUTYKH^{3,4} and Nasser KESHAVERZ FARAJ KHAH⁵

¹ Institute of Geophysics, University of Tehran, Tehran, Iran

² Department of Earth Sciences, Uppsala University, Uppsala, Sweden

³ Univ. Grenoble Alpes, Univ. Savoie Mont Blanc, CNRS, LAMA, 73000 Chambéry, France

⁴ LAMA UMR 5127 CNRS, Université Savoie Mont Blanc, Campus Scientifique, 73376 Le Bourget-du-Lac, France

⁵ Research Institute of Petroleum Industry, Tehran, Iran

Abstract. The MAKRAN subduction zone, an approximate 1000 km section of the EURASIAN–ARABIAN plate, is located offshore of SOUTHERN IRAN and PAKISTAN. In 1945, the MAKRAN subduction zone (MSZ) generated a tsunamigenic earthquake with a magnitude of M_w 8.1. The region has also experienced large historical earthquakes but the data regarding these events are poorly documented. Therefore, the need to investigate tsunamis in MAKRAN must be taken into serious consideration. Using hydrodynamic numerical simulation, we evaluate the tsunami wave energy generated by bottom motion for a tsunamigenic source model distributed along the full length of the MAKRAN subduction zone. The whole rupture of the plate boundary is divided into 20 segments with width of order of 200 km and a co-seismic slip of 10 m but with various lengths. Exchanges between kinetic and potential components of tsunami wave energy are shown. The total tsunami wave energy displays only 0.33 % of the seismic energy released from the earthquake source. As a result, for every increase in magnitude by one unit, the associated tsunami wave energy becomes about 10^3 times greater.

Keywords: Tsunami wave; wave energy; co-seismic displacement; tsunami modeling; Makran region

1 Introduction

The catastrophic effects of the 2004 INDONESIA ($M_w \sim 9.1$) and 2011 JAPAN ($M_w \sim 9.0$) tsunamis motivated researchers to study different characteristics of tsunami waves. One of those characteristics is the tsunami wave energy. Tsunami wave energy includes the transformed part of seismic energy into the water. Computation of tsunami wave energy is a way to measure the power of tsunamis and reflects the potency of their generators. Tsunami wave energy has not been investigated as widely as other characteristics of tsunami *e.g.* travel time, amplitude, velocity, *etc.* Nevertheless, it has been discussed in some studies (Kajiura, 1970; Ward, 1980; Dotsenko and Korobkova, 1997; Velichko et al., 2002; Okal and Synolakis, 2003; Kowalik et al., 2007; López-Venegas et al., 2015; Omira et al., 2016). The far-field impacts of tsunamis caused by earthquakes are well understood (Ruiz et al., 2015). Estimating the seismic moment M_0 of a submarine earthquake is sufficient to compute the impact of tsunamis at far field, whereas evaluating the severity of near-field tsunamis is relatively controversial. Tsunami run-up distributions are used usually to measure the near-field effects of tsunamis which can be highly uncertain depending on several factors (Geist, 2002; Dutykh et al., 2011; Ruiz et al.,

* Corresponding author. E-mail address: amin.rashidi@ut.ac.ir (A. RASHIDI).

2015). The run-up heights and local tsunami amplitudes widely vary respecting the moment magnitude (M_w) of the associated earthquake (Dutykh et al., 2012). While run-up distributions along coastlines rely on site-specific conditions and local bathymetric variations, tsunami wave energy can be a better representative to understand the overall severity of local tsunamis.

The shallow great earthquakes at subduction zones generate the most destructive tsunamis (Satake and Tanioka, 1999). The subduction of ARABIAN plate beneath the EURASIAN plate in the northwestern INDIAN OCEAN has generated the MAKRAN subduction zone (MSZ) with a length of 900-1000 km. The rate of convergence increases from 2.3 cm/y in the western edge to 2.9 cm/y at the eastern boundary of MAKRAN (Regard et al., 2005), but with no obvious deep-sea trench (Schlüter et al., 2002). The MAKRAN subduction zone is seismically split into an active eastern and an apparently inactive western segment. The present-day offshore seismicity in the MAKRAN is generally low (Smith et al., 2012). Nevertheless, it generated a tsunamigenic earthquake on 1945 NOVEMBER 27, which triggered a significant regional tsunami with 11-13 m maximum run-up (Ambraseys and Melville, 1982; Okal and Synolakis, 2008; Shah-hosseini et al., 2011). This large height of run-up may indicate that a delayed triggered submarine landslide by the earthquake was involved as the possible cause of the tsunami amplification (Ambraseys and Melville, 1982; Heidarzadeh and Satake, 2017). Future earthquakes along the MAKRAN subduction zone can potentially trigger submarine landslides due to very thick sediments on the continental shelf which is in order of 7 km. Such submarine landslides will amplify the wave heights of local tsunamis as was observed. The data regarding the exact impacts of the 1945 tsunami on the coastlines are really limited; however, the reports suggest that the event caused remarkable destruction and about 4000 deaths (Heck, 1947; Ambraseys and Melville, 1982; Heidarzadeh et al., 2008). Similar events can reoccur by the MAKRAN subduction zone between about 125-250 years based on Page et al. (1979) computations. Byrne et al. (1992) mentioned that similar events can be repeated every 175 years in the eastern MAKRAN. Despite the very limited historical data, Quittmeyer and Jacob (1979) mentioned four possible large historical events in 1483, 1851, 1864 and 1765. There is no strong evidence to suggest that those events caused tsunamis. However, Ambraseys and Melville (1982) indicated that the 1765 event caused a tsunami (Zarifi, 2006). Byrne et al. (1992) approximated the rupture area of 1765, 1851 and 1945 large earthquakes (Figure 1). They considered the 1864 event to have occurred inside the 1851 rupture area since they impacted the same region. The 1483 event is considered as the only major event that may have occurred in the western MAKRAN. However, there are some studies on the coastal terraces suggesting that a probable earthquake on the western segment in 1008 AD caused about 2 m of uplift and a tsunami with about 4 m of wave heights (Ambraseys and Melville, 1982; Shah-hosseini et al., 2011; Frohling and Szeliga, 2016). There is no proof to accurately estimate the location of these events.

Despite the fact that understanding of the present tsunamigenic behavior of the MAKRAN subduction zone is complex, it is worth studying the tsunami properties in the MAKRAN region. Frohling and Szeliga (2016) using the GPS measurements concluded that the MAKRAN subduction zone is partly locked and accumulating strain. They inferred that sectional locking of the MSZ makes it capable of generat-

ing earthquakes up to M_w 8.8. The length of MSZ (900-1000 km) is about the same as SUMATRA 2004 mega-thrust earthquake rupture length (~ 1000 km) (Ammon et al., 2005). Assuming the locking of the MSZ, especially the western segment (Musson, 2009; Rajendran et al., 2013), it has potential to generate plate boundary earthquakes, hence tsunamis. Tsunami in the MAKRAN subduction zone will be a real threat to northern INDIAN OCEAN countries, especially IRAN, OMAN, PAKISTAN and INDIA. As the number of facilities and residences are increasing along shores of those countries, the exposure and vulnerability to tsunami hazard are also increasing.

In this study, we compute the energy of waves generated by sea floor motion for a tsunamigenic source model involving the full length of the MAKRAN subduction zone. The distribution of maximum tsunami amplitudes is also presented to evaluate the near-field tsunami hazard from the source model. Tsunami numerical modeling assists us in our computations.

2 Methodology

2.1 Tsunami wave energy

Very long tsunami waves lose little energy as they propagate from the generation area to coastlines and cause greater run-up than storm waves (Bryant, 2008). The strength of a tsunami depends on type and characteristics of the source. Tsunami energy is distributed all through the water column immediately after its generation. Stronger sources displace more volume of water, therefore cause more energetic tsunamis. Tsunamis generated by shallow undersea earthquakes are usually stronger than submarine landslide-generated tsunamis and lose less energy. The uplift motion of sea floor due to a subsurface rupturing immediately pushes up the sea water from the bottom and displaces the sea surface. The life-cycle of tsunami energy can be described in three general sequential phases (Dutykh and Dias, 2009); i) a portion of seismic energy is pumped into the ocean by bottom motion; ii) during the propagation stage kinetic and potential energies are constantly exchanged; iii) tsunami energy is used to inundate the coasts during wave run-up.

In this context, we compute tsunami energy based on Dutykh and Dias (2009) as they conducted a comprehensive theoretical investigation on the energy of tsunami waves generated by sea floor motion. Using the incompressible fluid dynamics equations, they drove the equation of energy E as the sum of kinetic K and potential Π energies. In the case of the free surface incompressible flows, the kinetic energy is based on the horizontal velocity field and the potential energy on the free surface elevation (Dutykh et al., 2012). Thus, summarizing it:

$$E(t) = K(t) + \Pi(t), \quad (1)$$

with

$$\Pi(t) = \frac{\rho g}{2} \iint_{\Omega} \eta^2 d\mathbf{x}, \quad K(t) = \frac{\rho}{2} \iint_{\Omega} H(u^2 + v^2) d\mathbf{x}, \quad \mathbf{x} \in \Omega, \quad (2)$$

where ρ is the ocean water density, g is the gravity acceleration, η denotes the free surface excursion (or elevation), H is the total water depth, u and v are horizontal

velocity components in X and Y directions respectively, and Ω stands for the physical domain (bathymetric domain). Note that Equations (1) and (2) are valid in the framework of nonlinear shallow water equations (long waves). Figure 2 shows the selected bathymetric domain in this study. The tsunami waves excited by a rupture source model are simulated to evaluate the energy.

2.2 Tsunami numerical model

To calculate the tsunami wave energy, numerical tsunami modeling is performed using the well-known COMCOT hydrodynamic model (Liu et al., 1998) where leap-frog time-differencing scheme is used to solve both linear and nonlinear shallow water equations on both CARTESIAN (XOY) and spherical ($\theta O \phi$) coordinate systems. The vertical sea floor displacement generated by submarine earthquakes is transferred to the water surface as the initial condition. The initial condition for performing the tsunami propagation modeling is computed using the OKADA solution (Okada, 1985). A tsunamigenic source model involving the full length of the MAKRAN subduction zone is constructed to perform the simulation as presented in Figure 2. The full rupture of the plate boundary is divided into 20 segments with width of order of 200 km and a co-seismic slip of 10 m (Smith et al., 2013) but with various lengths ranging from 27 to 72 km. Table 1 shows the fault parameters for each segment used in the modeling which are modified from Okal and Synolakis (2008) and Smith et al. (2013). A buried fault with top and bottom depths of fault at 12 km and 38 km is assumed.

<i>Parameter</i>	<i>Value</i>
Width (km)	210
Dip angle (°)	7
Slip angle (°)	90
Dislocation (m)	10
top depth (km)	12

Table 1. Fault parameters used for modeling the tsunami generation.

The common approach in the tsunami generation modeling is considering the static seabed deformation as the initial water surface. The duration of rupture process on the fault and thus the time dependence of the sea bottom displacement is neglected based on this approach. Figure 3 shows the vertical static deformation caused by the MAKRAN scenario. Taking into account the dynamic effect of rupture process of the fault, we define the activation time of each sub-fault t_i required for the rupture to achieve the corresponding segment i using the formula (Dutykh et al., 2012):

$$t_i = \frac{\|\chi_e - \chi_i\|}{\nu_r}, \quad i = 1, \dots, N_x \times N_y, \quad (3)$$

where χ_e and χ_i stand for hypo-center and i^{th} sub-fault locations. In Equation (3), ν_r is the rupture velocity, N_x and N_y denote for the number of sub-faults down

the dip angle and along strike, respectively. The norm in Equation (3) is Euclidean. For the sake of simplicity, we presume that the rupture starts from the centroid of the first segment and propagates in both along-strike and the opposite directions. Assuming a rupture velocity of 1.5 km/s, the total rupture duration is about 600 s. The passive generation is used for each segment, but we put some dynamics nevertheless, thanks to the rupture propagation time. The OKADA solution (Okada, 1985) is used for computing the vertical seabed deformation. The evolution of the seabed deformation for dynamic stages is shown in Figure 4. It can be seen that no subsidence occurs seaward for both static and dynamic bottom motions which reflects leading elevation waves. The maximum uplift in both cases is about 4 m. The GEBCO 1 – min bathymetry data (available at <http://www.gebco.net/>) is used for our simulations. The simulations are conducted using a time step of 2 s. Nonlinear shallow water equations in spherical coordinates are taken in the calculation.

3 Results

Figures 5-7 show distributions of water surface elevation, total energy density, potential energy density and kinetic energy density at different times for static and dynamic scenarios. Tsunami energy emits primarily at right angles to the fault (Kajiura, 1970; Ben-Menahem and Rosenman, 1972). The redistribution of tsunami energy into potential and kinetic components and the exchanges between them at different times can be seen. The evolution of total energy and its potential and kinetic components is shown in Figure 8. Tsunami wave energy decreases with time. Under the ideal conditions, the total energy remains constant after the sea floor deformation process is done (Dutykh and Dias, 2009). However, the energy is attenuated due to some factors that can dissipate it *e.g.* numerical diffusion, bottom friction, run-up, *etc.*

Figure 9 shows the relation between moment magnitude M_w and computed tsunami wave energy E for the entire MAKRAN, western MAKRAN and eastern MAKRAN based on our simulations. The averaged equation for the magnitude-energy relationship can be given by:

$$\lg E = 2.98 \cdot M_w - 11.49. \quad (4)$$

It can be seen that the magnitude correlates with tsunami energy linearly. However, the relationship is relatively different for different scenarios. Equation (4) indicates that for every increase in magnitude by one unit, the associated tsunami wave energy released becomes about 10^3 times greater.

Figure 10 presents the distributions of maximum positive amplitudes in the simulation duration of 10 h. Differences between results of three rupture scenarios are negligible. They all express an obvious local risk posed to the shores of IRAN, PAKISTAN and OMAN. A relative contrast between maximum amplitudes in the GULF of OMAN and the ARABIAN SEA where the MURRAY ridge is located can be seen. The maximum tsunami wave amplitude from earthquake sources varies from 0 to 8 m inside the computational domain. Due to lack of high-resolution local bathymetry/topography maps, tsunami inundation and run-up on dry land are not contributed in this study.

We also computed time-series at four selected virtual gauges (see Figure 11). The results show minor differences in arrival times and amplitudes of earthquake scenarios. The results slightly show the azimuthal dependence of the arrival times and amplitudes. The scenario with rupture propagation along the strike causes larger maximum height than other scenarios at HORMUZ. Tsunami waves generated from this scenario arrive at HORMUZ later than other scenarios. A greater maximum water height is produced at MUMBAI by the scenario with rupture propagation from left to right. The arrival time of tsunami waves from this scenario at MUMBAI is longer than other scenarios. Tsunami waves rapidly arrive at JIWANI. The water surface reaches its highest level at JIWANI after about 20 min. It takes about 15 min, 2 h and 4 h for tsunami waves to arrive at SUR, HORMUZ and MUMBAI respectively. The first tsunami peak at all stations is the highest wave. The maximum water elevations from various scenarios are about 1.5, 3.5, 0.5 and 4 m at HORMUZ, JIWANI, MUMBAI and SUR, respectively. It can be seen that the period of the largest tsunami waves arrived at HORMUZ is about 4 h, very longer than the typical tsunami waves period.

4 Discussion

The sea floor topography distributes tsunami wave crests and disperses energy in a larger area (Bryant, 2008). Higher amounts of the wave energy tend to concentrate at the leading edge of the tsunami waves. As tsunami waves reach the shallow water areas, their velocities are decreased but their amplitudes are enhanced. This leads to stronger kinetic energy and weaker potential energy. However, the total energy decreases. The dissipation of energy inside the GULF of OMAN occurs faster and higher than the ARABIAN SEA. Both dynamic scenarios radiate energy in a similar pattern but in opposite directions. Early, tsunami energy from the static scenario is distributed in a wider area having larger amounts of kinetic, potential and total energies, compared with dynamic scenarios. In the case of dynamic scenarios, tsunami energy is distributed only in the vicinity of the rupture zone before the completion of seabed deformation. Then it spreads out geometrically quickly. Later the distribution of tsunami energy generated by dynamic scenarios shows a similar pattern to energy from the static scenario. The exchanges between potential and kinetic energies can be clearly seen (see Figures 5–8). Once the sea floor deformation stops, the potential energy starts to decrease. In the case of static bottom motion, this process occurs immediately after instantaneous bottom motion. In the case of dynamic bottom motions, the potential energy increases until the rupture is complete over the fault. It constitutes the main proportion of total energy until the transient equipartition is reached. Then the kinetic energy is the dominant component of total energy. Tsunami waves retain their kinetic energy to impact the shores.

The MAKRAN source model is capable of generating a M_w 9.1 earthquake. Obviously, earthquakes with various sizes cause different levels of energy. As pointed out by Ward (1980), it is not possible to have a unique relationship between tsunami energy and earthquake size. However, the relationship can be obtained for every source. The maximum level of total energy (Figure 8) is considered as the value of tsunami wave energy radiated which is 2.9×10^{15} J for the static scenario and is

$3.0 \times 10^{15} \text{ J}$ for both dynamic scenarios. The radiated seismic energy E_S (Choy and Boatwright, 1995) for the source model is $9.0 \times 10^{17} \text{ J}$. Therefore, only 0.33% of the seismic energy transmits to the tsunami energy. As shown by Ward (1980), 0.1% to 1% of the energy released in earthquakes normally transmits to a tsunami.

The effects of tsunamis on the shorelines of IRAN and OMAN is rather higher than PAKISTAN (Figure 10). The trapped waves, produced by the western segment, inside the GULF of OMAN can cause high local waves. The tsunami wave amplitudes are weakened to the west of GULF of OMAN around the STRAIT of HORMUZ. The tsunami waves energy and the velocity of tsunami waves are highly attenuated as they pass the STRAIT of HORMUZ and enter the PERSIAN GULF. This led to weaker and less energetic tsunami waves which makes the PERSIAN GULF very safer than GULF of OMAN against tsunamis.

We would like to stress out that estimations presented in our study are rather conservative. One of the main sources of uncertainties for the tsunamigenic potential of MSZ is the presence of thick sedimentary layers. The behavior of sedimentary layers during an earthquake is quite difficult to predict. Sediments may trigger landslides that will amplify locally tsunami waves. This effect remains extremely uncertain. Furthermore, they can act as springs to amplify the vertical seabed displacement due to an earthquake as it was clearly demonstrated in (Dutykh and Dias, 2010). Therefore, the presence of thick sediments may have undeniable implications on the tsunami hazard from the possible future events in the MSZ.

5 Conclusions

A useful concept in measuring the degree of tsunamis is to seek the amount of the energy of waves generated by sea floor displacement. In this study, the generated wave energy is estimated for a hypothetical tsunamigenic source based on numerical modeling. Both static and dynamic bottom motions are considered as tsunami generation statuses. The maximum amplitude fields from them show minor differences. The partition of energy between potential and kinetic energies is obvious during its evolution. Total tsunami energy decreases with time indicating that it is not constant once the sea floor deformation stops. While the potential energy of tsunami waves weakens, the kinetic component of energy becomes stable after a while to impact the coasts. The ratio percentage of tsunami wave energy and radiated seismic energy is $E/E_S = 0.33$. The relation between magnitude and tsunami wave energy is given. For every increase of one unit of magnitude, the relative increase of tsunami wave energy of about 1000 times.

References

- Ambraseys, N. N., Melville, C. P., 1982. A History of Persian Earthquakes. Cambridge Earth Science Series. Cambridge University Press. 2
- Ammon, C. J., Ji, C., Thio, H.-K., Robinson, D., Ni, S., Hjorleifsdottir, V., Kanamori, H., Lay, T., Das, S., Helmberger, D., Ichinose, G., Polet, J., Wald, D., 2005. Rupture process of the 2004 sumatra-andaman earthquake. Science 308 (5725), 1133–1139. 3

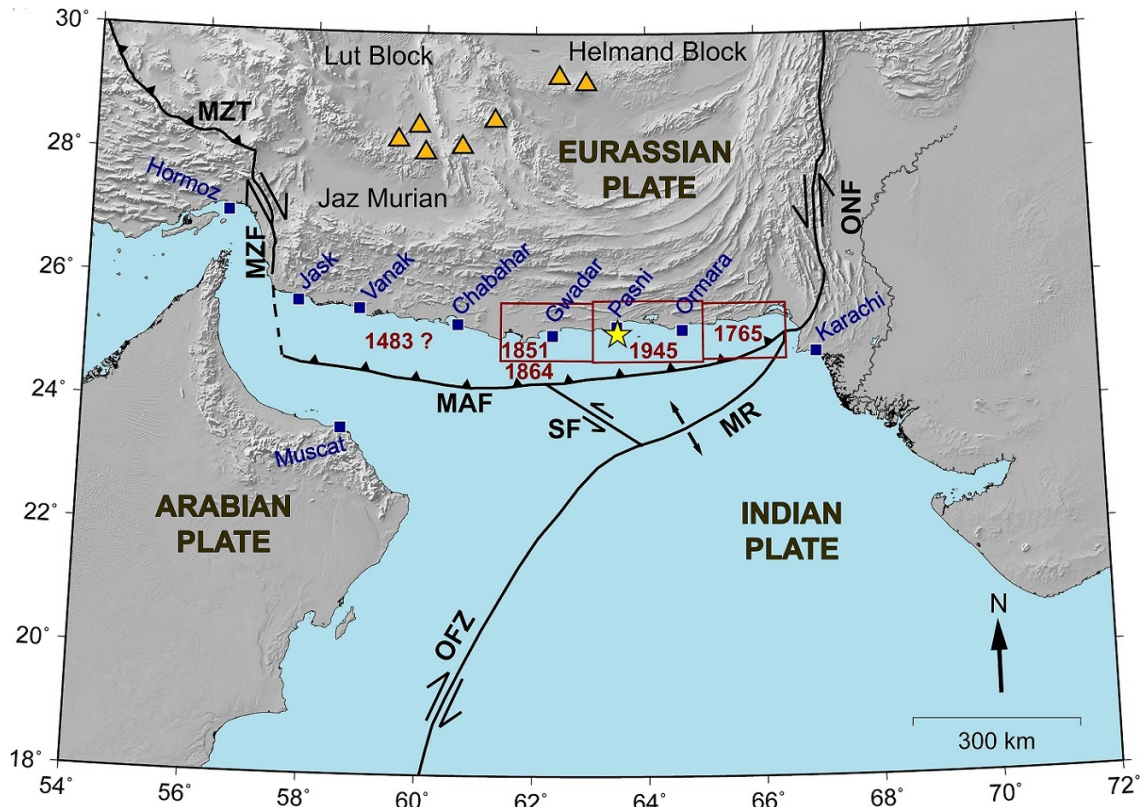


Fig. 1. Tectonic features of the MAKRAN region. MAF MAKRAN accretionary front, SF SONNE fault, MZF MINAB-ZENDAN fault, MZT main ZAGROS fault, OFZ OWEN fault zone. The triangles denote the volcanoes. The yellow star shows the epicenter of 1945 earthquake. The three blocks stand for the possible rupture areas of 1851 (1864), 1945 and 1765 earthquakes based on *Byrne et al. (1992)*.

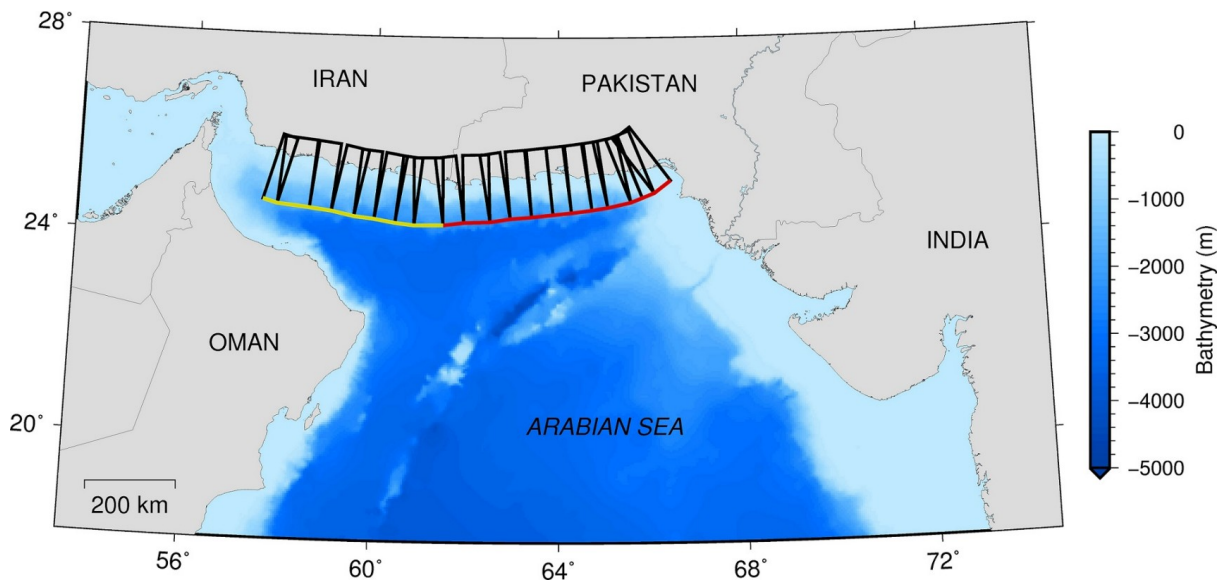


Fig. 2. The tsunami source model for the MAKRAN subduction zone. The yellow and red lines separate the western and eastern segments of the MAKRAN subduction zone. The rupture model includes 20 segments with width of order of 200 km and various lengths ranging from 27 to 72 km.

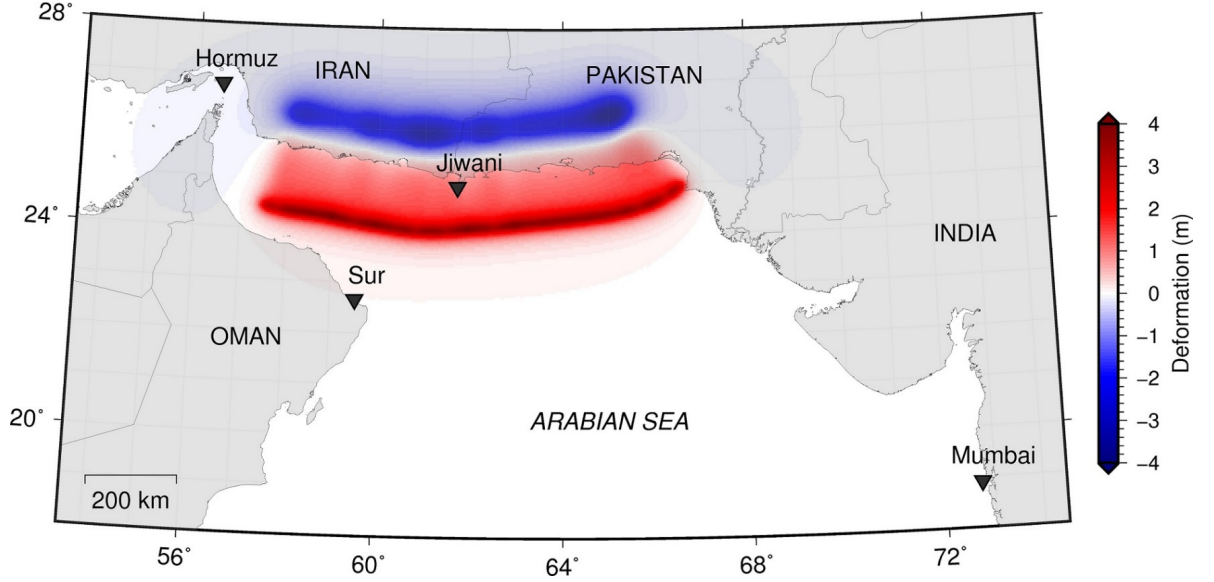


Fig. 3. The static deformation generated by the MAKRAN source model. Inverted triangles show the locations of the virtual gauges.

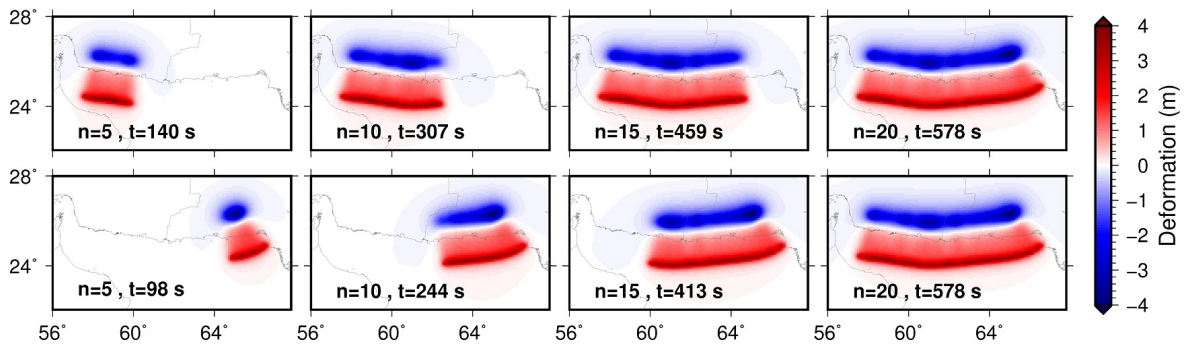


Fig. 4. The evolution of dynamic seabed deformation generated by the MAKRAN source model when rupture propagates in the along-strike (bottom frame) and the opposite (top frame) directions with $\nu_r = 1.5$ km/s. Variables n and t stand for the number of activated segments and the associated time (s) respectively.

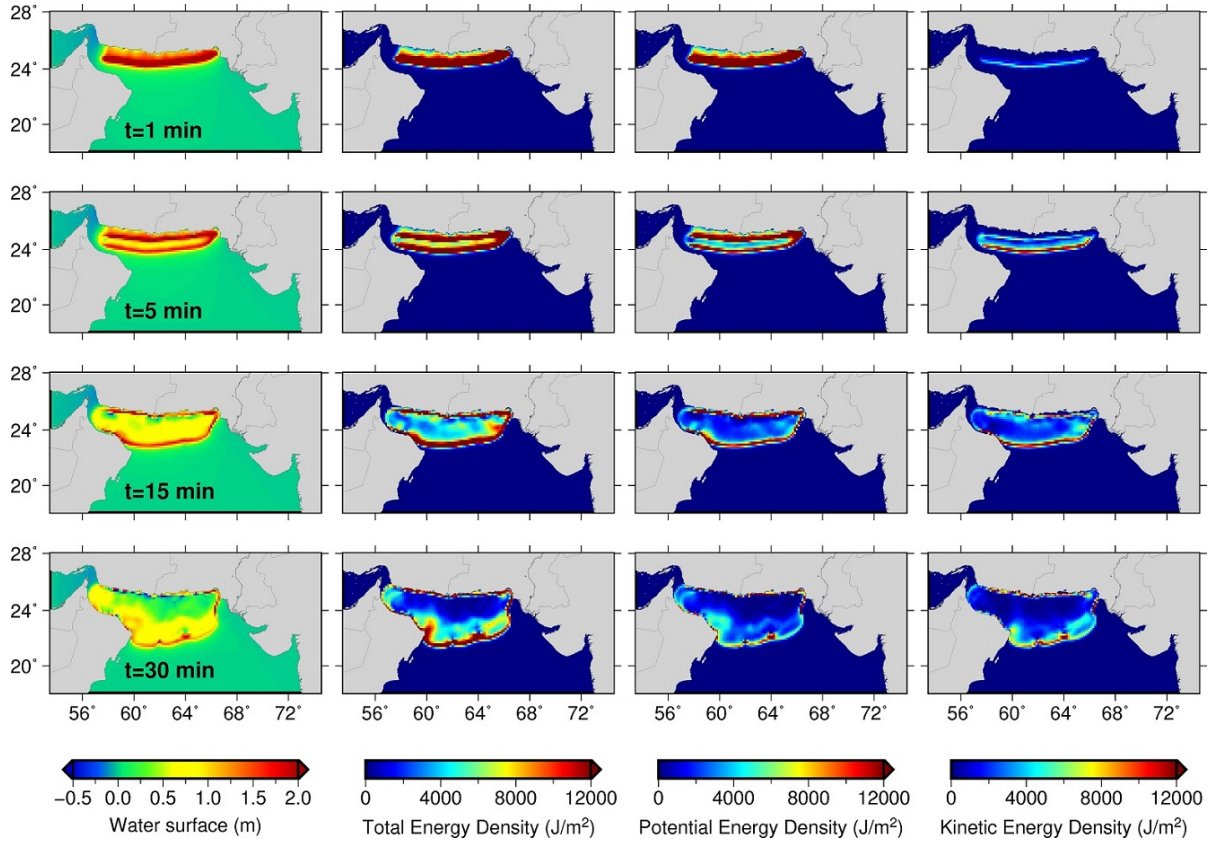


Fig. 5. Distributions of free surface elevation, total energy density, potential energy density and kinetic energy density at various times for the static scenario.

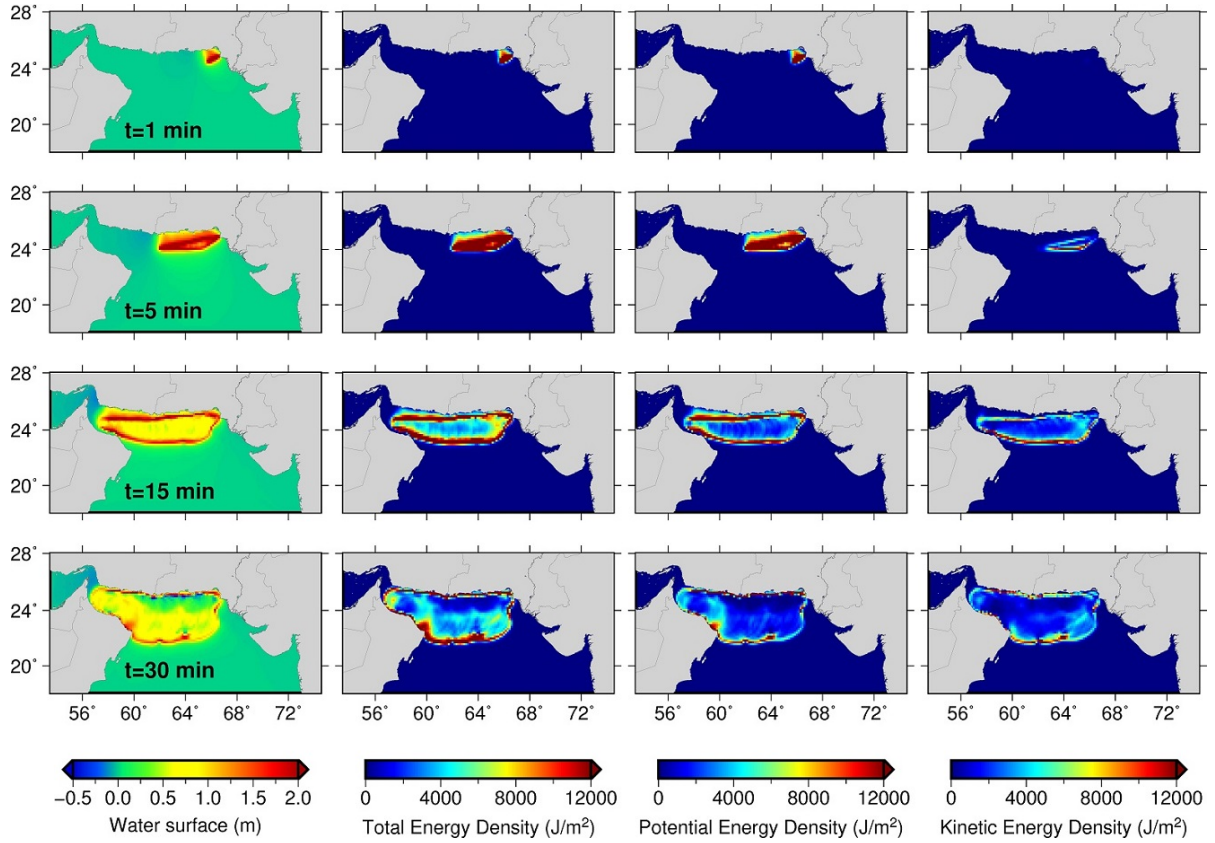


Fig. 6. Same as Figure 5 for the dynamic scenario with rupture propagation along the strike.

- Ben-Menahem, A., Rosenman, M., 1972. Amplitude patterns of tsunami waves from submarine earthquakes. *J. Geophys. Res.* 77, 3097–3128. [5](#)
- Bryant, E., 2008. *Tsunami: The Underrated Hazard*. Springer Praxis Books. Springer Berlin Heidelberg. [3](#), [6](#)
- Byrne, D. E., Sykes, L. R., Davis, D. M., 1992. Great thrust earthquakes and aseismic slip along the plate boundary of the Makran Subduction Zone. *J. Geophys. Res.* 97 (B1), 449–478. [2](#), [8](#)
- Choy, G. L., Boatwright, J. L., 1995. Global patterns of radiated seismic energy and apparent stress. *J. Geophys. Res.* 100 (B9), 18205–18228. [7](#)
- Dotsenko, S. F., Korobkova, T. Y., 1997. The effect of frequency dispersion on plane waves generated as a result of bed motions. *Phys. Oceanogr.* 8(3), 143–154. [1](#)
- Dutykh, D., Dias, F., 2009. Energy of tsunami waves generated by bottom motion. *Proc. R. Soc. A* 465, 725–744. [3](#), [5](#)
- Dutykh, D., Dias, F., 2010. Influence of sedimentary layering on tsunami generation. *Comput. Methods Appl. Mech. Eng.* 199 (21–22), 1268–1275. [7](#)
- Dutykh, D., Labart, C., Mitsotakis, D., 2011. Long wave run-up on random beaches. *Phys. Rev. Lett.* 107, 184504. [1](#)
- Dutykh, D., Mitsotakis, D., Chubarov, L. B., Shokin, Y. I., 2012. On the contribution of the horizontal sea-bed displacements into the tsunami generation process. *Ocean Modelling* 56, 43–56. [2](#), [3](#), [4](#)
- Frohling, E., Szeliga, W., 2016. GPS constraints on interplate locking within the Makran subduction zone. *Geophys. J. Int.* 205 (1), 67–76. [2](#)

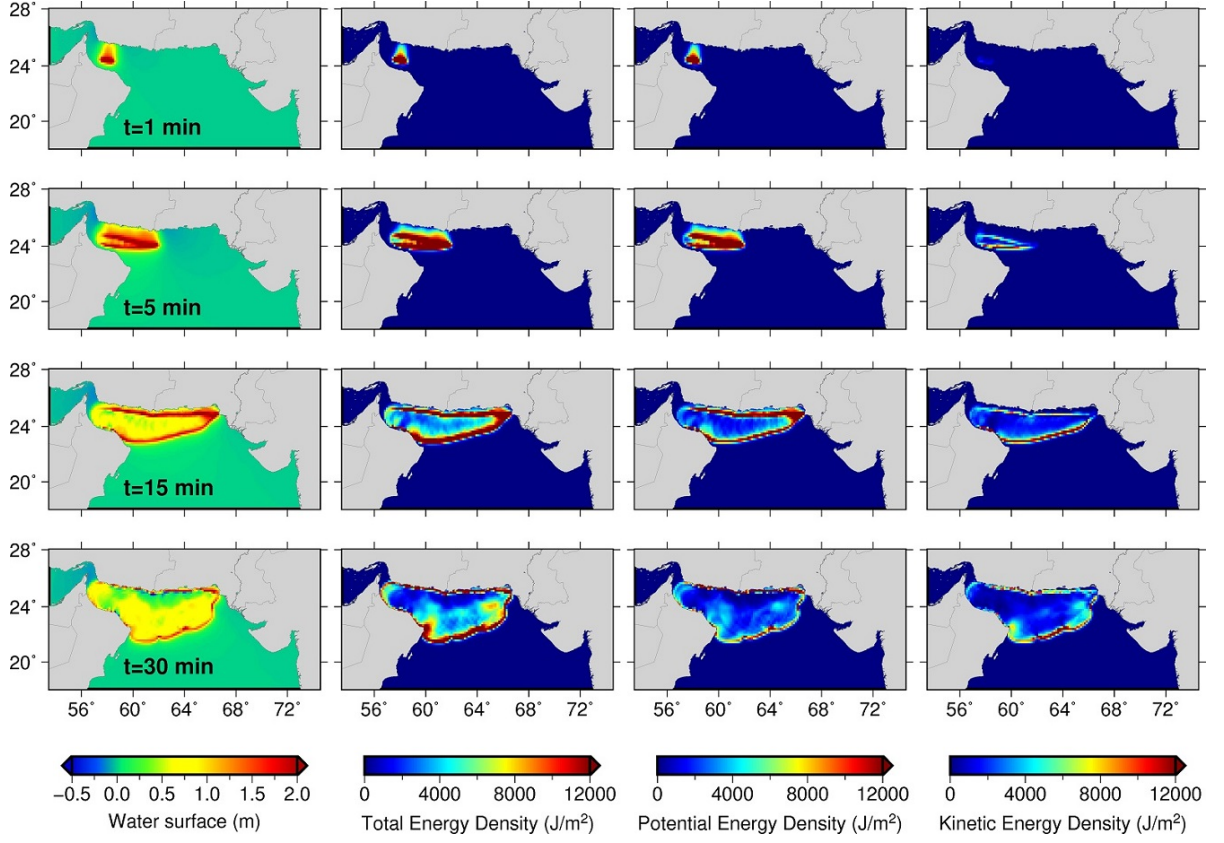


Fig. 7. Same as Figure 5 but for the dynamic scenario with rupture propagation in the opposite along-strike direction.

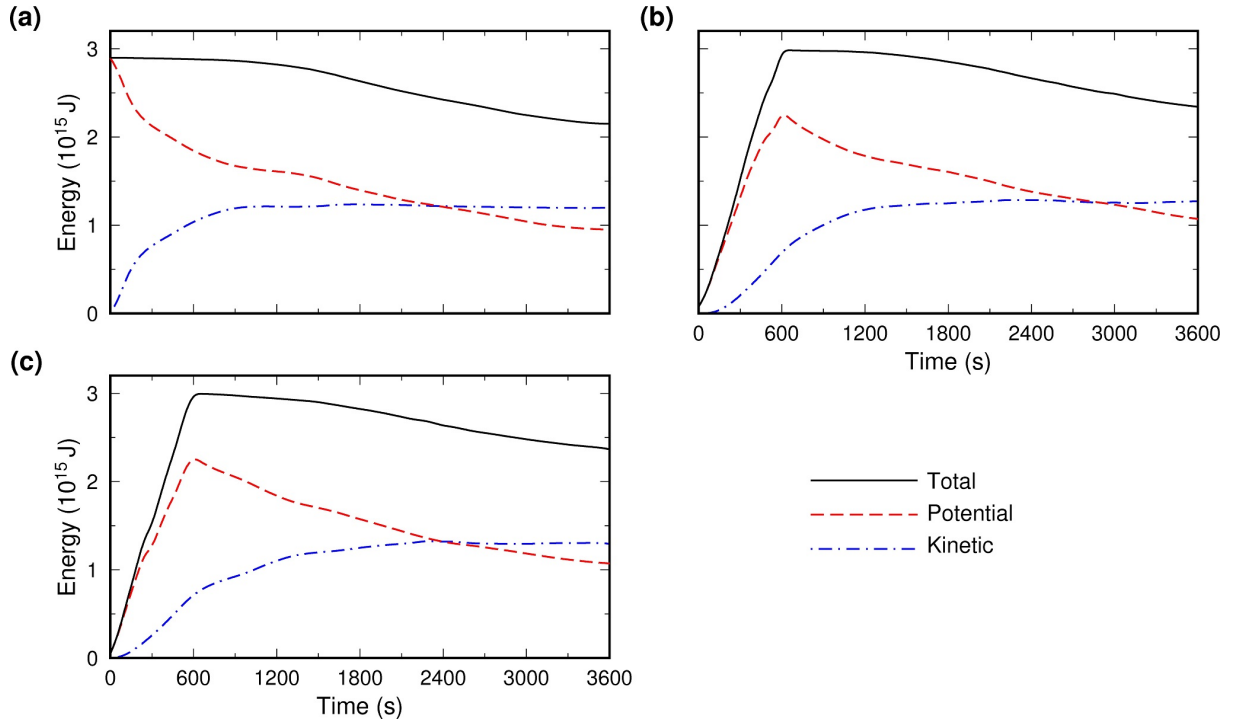


Fig. 8. Energy as a function of time computed for static scenario (a) and dynamic scenarios with rupture propagation in the along-strike (b) and opposite along-strike (c) directions. In each figure, black, red dashed and blue dot-dashed curves represent total, potential and kinetic energies respectively.

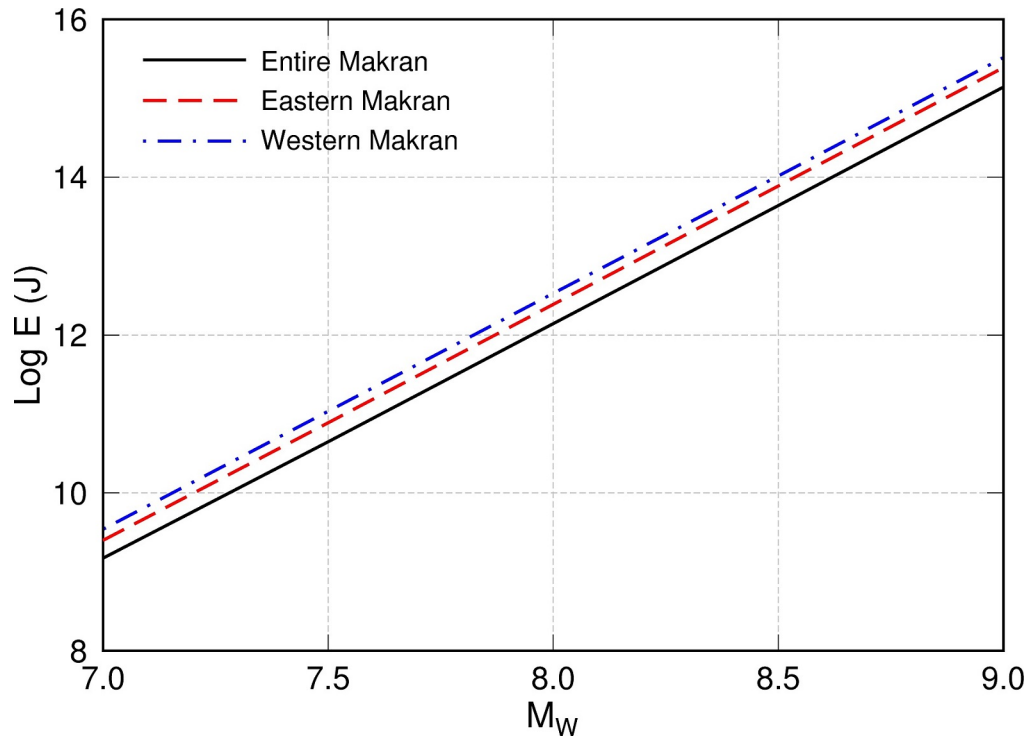


Fig. 9. Relationship between tsunami wave energy and moment magnitude for the entire MAKRAN (black curve), western MAKRAN (blue dot-dashed curve) and eastern MAKRAN (red dashed curve) based on our simulations.

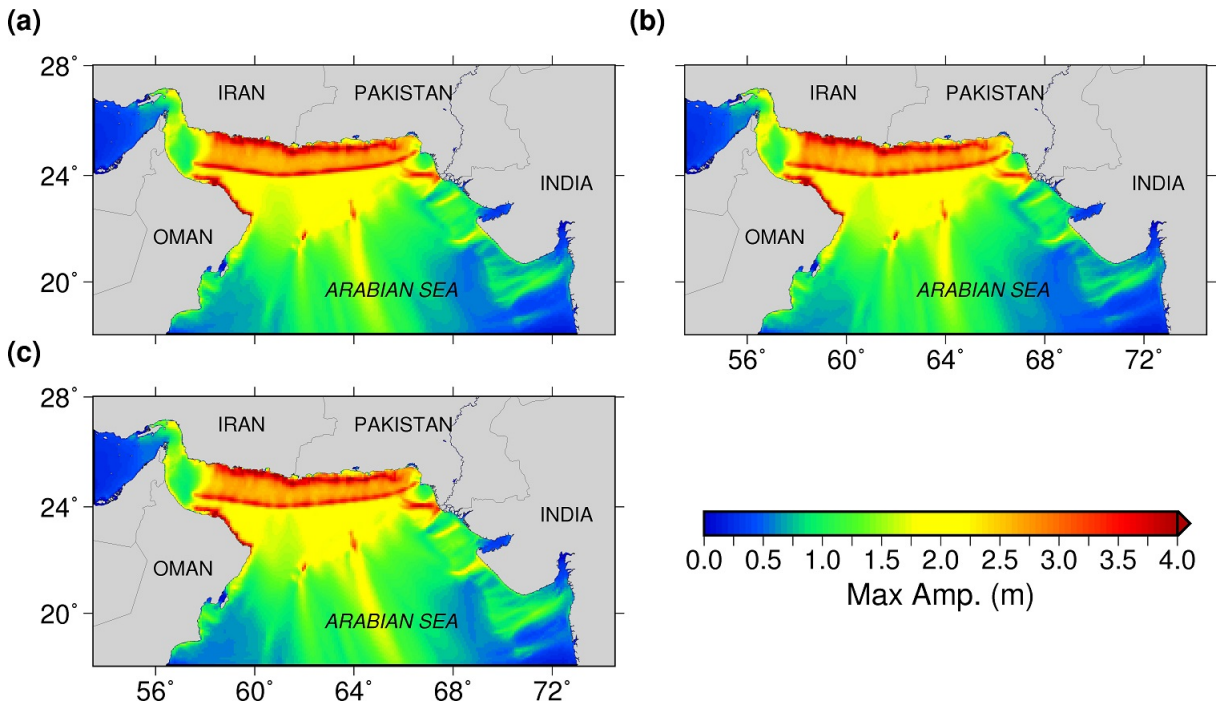


Fig. 10. Maximum wave amplitude from static scenario (a) and dynamic scenarios with rupture propagation in the along-strike (b) and opposite along-strike (c) directions.

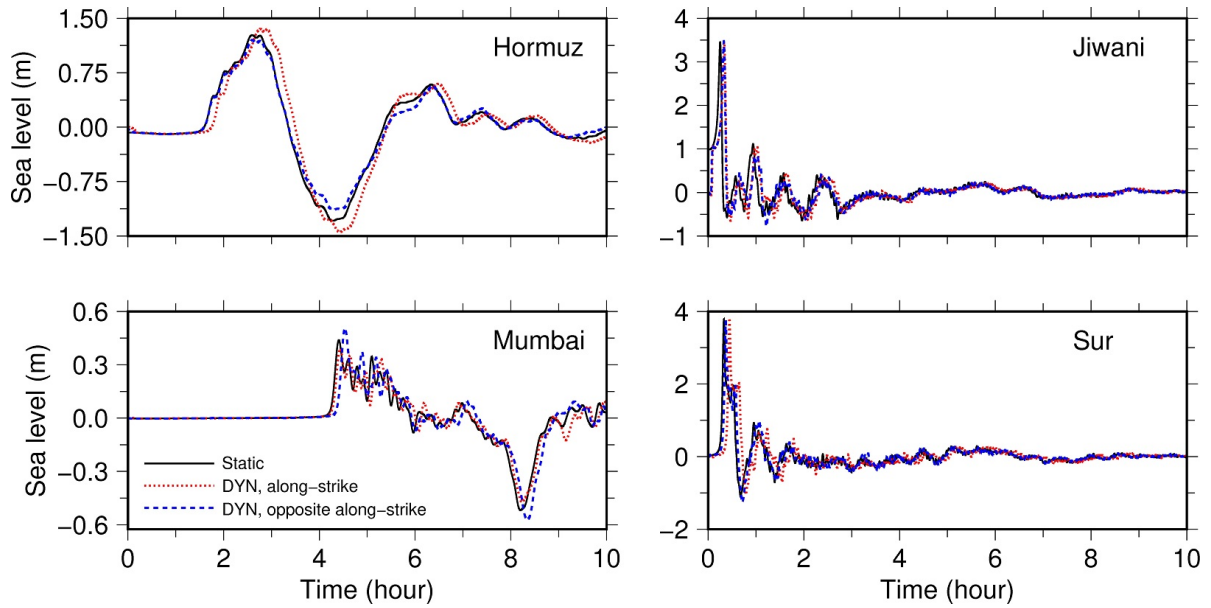


Fig. 11. Computed waveforms at four gauges (HORMUZ, JIWANI, MUMBAI and SUR) from static scenario (black curve), dynamic scenarios with rupture propagation in the along-strike (red dotted curve) and opposite along-strike (blue dashed curve) directions. DYN dynamic.

- Geist, E., 2002. Complex earthquake rupture and local tsunamis. *J. Geophys. Res.* 107, B5. [1](#)
- Heck, N. H., 1947. List of seismic sea waves. *Bull. Seism. Soc. Am.* 37 (4), 269–286. [2](#)
- Heidarzadeh, M., Pirooz, M. D., Zaker, N. H., Yalciner, A. C., Mokhtari, M., Esmaeily, A., 2008. Historical tsunami in the Makran Subduction Zone off the southern coasts of Iran and Pakistan and results of numerical modeling. *Ocean Engineering* 35 (8-9), 774–786. [2](#)
- Heidarzadeh, M., Satake, K., 2017. A Combined Earthquake–Landslide Source Model for the Tsunami from the 27 November 1945 Mw 8.1 Makran Earthquake. *Bull. Seism. Soc. Am.* 107 (2), 1033–1040. [2](#)
- Kajiura, K., 1970. Tsunami source, energy and the directivity of wave radiation. *Bull. Earthquake Res. Inst., Tokyo Univ.* 48, 835–869. [1](#), [5](#)
- Kowalik, Z., Knight, W., Logan, T., Whitmore, P., 2007. The tsunami of 26 December, 2004: Numerical modeling and energy considerations. *Pure Appl. Geophys.* 164, 379–393. [1](#)
- Liu, P. L.-F., Woo, S.-B., Cho, Y.-K., 1998. Computer Programs for Tsunami Propagation and Inundation. Tech. rep., School of Civil and Environmental Engineering, Cornell University. [4](#)
- López-Venegas, A. M., Horrillo, J., Pampell-Manis, A., Huérfano, V., Mercado, A., 2015. Advanced Tsunami Numerical Simulations and Energy Considerations by use of 3D–2D Coupled Models: The October 11, 1918, Mona Passage Tsunami. *Pure Appl. Geophys.* 172 (6), 1679–1698. [1](#)
- Musson, R. M. W., 2009. Subduction in the Western Makran: the historian’s contribution. *J. Geol. Soc. London* 166 (3), 387–391. [3](#)
- Okada, Y., 1985. Surface deformation due to shear and tensile faults in a half-space. *Bull. Seism. Soc. Am.* 75, 1135–1154. [4](#), [5](#)

- Okal, E. A., Synolakis, C. E., 2003. A theoretical comparison of tsunamis from dislocations and landslides. *Pure Appl. Geophys.* 160, 2177–2188. [1](#)
- Okal, E. A., Synolakis, C. E., 2008. Far-field tsunami hazard from mega-thrust earthquakes in the Indian Ocean. *Geophys. J. Int.* 172, 995–1015. [2](#), [4](#)
- Omira, R., Baptista, M. A., Lisboa, F., 2016. Tsunami Characteristics Along the Peru–Chile Trench: Analysis of the 2015 Mw8.3 Illapel, the 2014 Mw8.2 Iquique and the 2010 Mw8.8 Maule Tsunamis in the Near-field. *Pure Appl. Geophys.* 173 (4), 1063–1077. [1](#)
- Page, W. D., Alt, J. N., Cluff, L. S., Plafker, G., 1979. Evidence for the recurrence of large-magnitude earthquakes along the Makran coast of Iran and Pakistan. *Tectonophysics* 52 (1), 533–547. [2](#)
- Quittmeyer, R. C., Jacob, K. H., 1979. Historical and modern seismicity of Pakistan, Afghanistan, northwestern India, and southeastern Iran. *Bull. Seism. Soc. Am.* 69 (3), 773–823. [2](#)
- Rajendran, C. P., Rajendran, K., Shah-hosseini, M., Beni, A. N., Nautiyal, C. M., Andrews, R., 2013. The hazard potential of the western segment of the Makran subduction zone, northern Arabian Sea. *Natural Hazards* 65 (1), 219–239. [3](#)
- Regard, V., Bellier, O., Thomas, J.-C., Bours, D., Bonnet, S., Abbassi, M. R., Braucher, R., Mercier, J., Shabanian, E., Soleymani, S., Feghhi, K., 2005. Cumulative right-lateral fault slip rate across the Zagros–Makran transfer zone: role of the Minab–Zendan fault system in accommodating Arabia–Eurasia convergence in southeast Iran. *Geophys. J. Int.* 162 (1), 177–203. [2](#)
- Ruiz, J. A., Fuentes, M., Riquelme, S., Campos, J., Cisternas, A., 2015. Numerical simulation of tsunami runup in northern Chile based on non-uniform k-2 slip distributions. *Natural Hazards* 79 (2), 1177–1198. [1](#)
- Satake, K., Tanioka, Y., 1999. Sources of Tsunami and Tsunamigenic Earthquakes in Subduction Zones. *Pure Appl. Geophys.* 154 (3), 467–483. [2](#)
- Schlüter, H. U., Prexl, A., Gaedicke, C., Roeser, H., Reichert, C., Meyer, H., von Daniels, C., 2002. The Makran accretionary wedge: sediment thicknesses and ages and the origin of mud volcanoes. *Mar. Geol.* 185 (3), 219–232. [2](#)
- Shah-hosseini, M., Morhange, C., Beni, A. N., Marriner, N., Lahijani, H., Hamzeh, M., Sabatier, F., 2011. Coastal boulders as evidence for high-energy waves on the Iranian coast of Makran. *Mar. Geol.* 290 (1), 17–28. [2](#)
- Smith, G., McNeill, L., Henstock, T. J., Bull, J., 2012. The structure and fault activity of the Makran accretionary prism. *J. Geophys. Res.* 117 (B07407). [2](#)
- Smith, G. L., McNeill, L. C., Wang, K., He, J., Henstock, T. J., 2013. Thermal structure and megathrust seismogenic potential of the Makran subduction zone. *Geophys. Res. Letts.* 40 (8), 1528–1533. [4](#)
- Velichko, A. S., Dotsenko, S. F., Potetyunko, E. N., 2002. Amplitude-energy characteristics of tsunami waves for various types of seismic sources generating them. *Phys. Oceanogr.* 12(6), 308–322. [1](#)
- Ward, S. N., 1980. Relationship of tsunami generation and an earthquake source. *J. Phys. Earth* 28, 441–474. [1](#), [6](#), [7](#)
- Zarifi, Z., 2006. Unusual subduction zones : Case studies in Colombia and Iran. Ph.D. thesis, University of Bergen, Norway. [2](#)